

# Direct measurement of gaussian distributed radial crystallographic orientations of polycrystalline, layered-oxide secondary particles and their impact on materials utilization in battery cathodes

Julian Wegener<sup>a,b,\*</sup>, Levin Chee Xian Ho<sup>a,c</sup>, Vedran Glavas<sup>a</sup>, Jonathan Edward Mueller<sup>a</sup>, Sören Höhn<sup>d</sup>, André Clausner<sup>d</sup>, Arnulf Latz<sup>e,f,b,\*</sup>

<sup>a</sup> Volkswagen Group Innovation, Wolfsburg, Germany

<sup>b</sup> Institute of Electrochemistry, University of Ulm, Albert-Einstein-Allee 47, 89081 Ulm, Germany

<sup>c</sup> Institute of Electro and Information Technology, Hanover University of Applied Sciences and Arts, Ricklinger Stadtweg 120, 30459 Hanover, Germany

<sup>d</sup> Fraunhofer Institute for Ceramic Technologies and Systems IKTS, Winterbergstrasse 28, 01277 Dresden, Germany

<sup>e</sup> Helmholtz Institute Ulm for Electrochemical Energy Storage (HIU), 89081 Ulm, Germany

<sup>f</sup> Institute of Engineering Thermodynamics, German Aerospace Center (DLR), Pfaffenwaldring 38–40, 70569 Stuttgart, Germany

## ARTICLE INFO

### Keywords:

Lithium-ion batteries  
Polycrystalline secondary particle  
Layered oxides with anisotropic diffusion  
Electron backscatter diffraction (EBSD)  
3D Electrochemical simulation

## ABSTRACT

The sub-microstructure of polycrystalline lithium nickel manganese cobalt oxide ( $\text{Li}[\text{Ni}_x\text{Mn}_y\text{Co}_{1-x-y}]\text{O}_2$ , abbr. NMC) secondary particles is determined by the arrangement, morphology and crystallographic orientation of the primary particles and strongly impacts their capacity, rate capability and aging. Although most electrochemical models do not resolve the sub-microstructure, understanding the relationship between a secondary particle's sub-microstructure and its electrochemical behavior is essential for the rational design of advanced secondary particles. In this paper we investigate the sub-microstructure of polycrystalline NMC secondary particles both experimentally and computationally. Experimentally, electron backscatter diffraction (EBSD) measurements characterize the crystallography of the primary particles and a radial orientation of the a-b diffusion planes of the individual atomically layered  $\text{Li}[\text{Ni}_{0.6}\text{Mn}_{0.2}\text{Co}_{0.2}]\text{O}_2$  (NMC622, Ni-rich) primary particles, revealing a Gaussian distribution. Computationally, three-dimensional electrochemical simulations of polycrystalline secondary particles model the impact of the crystallographic orientation of the primary particles on the secondary particle's capacity. These simulations predict that the investigated NMC secondary particles have a capacity at a discharge rate of 1 C that is up to 8% higher than that of a randomly oriented material. This shows that the crystallographic orientations of polycrystalline secondary particles have a severe impact on the utilization of NMC particles.

## 1. Introduction

In 2019, M. Stanley Whittingham, John B. Goodenough and Akira Yoshino were awarded the Nobel Prize for their research on lithium ion battery technology [1] and thus for their major impact on technological progress. Although lithium ion batteries are already widely used for energy storage in mobile devices, much effort continues to be invested in the further development of rechargeable batteries. Indeed, the enormous potential of the rapidly growing electromobility market is providing new impetus for diverse research activities aimed at advancing lithium ion battery technology. Investigations of battery cells, components or materials typically focus on one of the length scales displayed in Fig. 1.

The composite of active material, binder and additives is commonly referred to as the microstructure of an electrode (see microscale in

Fig. 1) and is traditionally modeled by treating the active material as made up of homogeneous particles. On the cathode side, these particles are usually called secondary particles and have spherical shapes with a diameter in the order of 10 microns. Thus, typical length scales for the microstructure regime roughly correspond to the combined dimensions of the secondary particles being treated (typically  $\sim 100\text{s } \mu\text{m}$ ). When it comes to optimizing the performance of lithium ion batteries many experimental and theoretical studies have been performed in order to understand how the microstructure of the electrodes influences the energy density, fast charging behavior, aging mechanisms, cost efficiency and safety [2–8]. Nevertheless, many of these behaviors are influenced by structural features too small to be resolved on the scale of typical microstructure models.

In contrast, the sub microstructure (see sub microscale in Fig. 1) describes the characteristics of single active material secondary particles,

\* Corresponding author.

E-mail addresses: julian.wegener1@volkswagen.de (J. Wegener), arnulf.latz@dlr.de (A. Latz).

## Nomenclature

Roman symbols	Descriptions (Unit)
$a, b, c$	Crystal lattice parameters (nm)
$\bar{u}$	c axis of the NMC crystal (dimensionless)
$\bar{v}$	Radial reference orientation (dimensionless)
$f$	Probability density function of intrinsic sine behavior (dimensionless)
$g$	Sum of two Gaussian distributions (dimensionless)
$p^\circ$	Probability density distribution of $\Delta\alpha^\circ$ (dimensionless)
$p'$	Probability distribution of $\Delta\alpha^\circ$ normalized w.r.t. intrinsic sine (dimensionless)
$p^*$	Probability distribution of $\Delta\alpha$ (dimensionless)
$p$	Probability density distribution of $\Delta\alpha$ (dimensionless)
$c_{1,2}$	Fitting constants of Gaussian distribution (dimensionless)
$d_{offset}$	Distance between cross section and equatorial plane (m)
$G_i$	Predicted value of a statistical distribution (dimensionless)
$P_i$	Measured value of a statistical distribution (dimensionless)
$c_e$	Concentration of lithium ions in the electrolyte ( $\text{mol m}^{-3}$ )
$N_+$	Flux of lithium ions ( $\text{mol m}^{-2}\text{s}^{-1}$ )
$D_e$	Lithium ion diffusion coefficient in the electrolyte ( $\text{m}^2\text{s}^{-1}$ )
$t_+$	Transference number of lithium ions (dimensionless)
$z_+$	Charge number of lithium ions (dimensionless)
$F$	Faraday constant, $96485 \text{ C mol}^{-1}$
$\vec{j}$	Electrical current density ( $\text{A m}^{-2}$ )
$c_s$	Concentration of lithium ions in active materials ( $\text{mol m}^{-3}$ )
$D_s$	Lithium ion diffusion coefficient in the active materials ( $\text{m}^2\text{s}^{-1}$ )
$i_{00}$	Scale of Butler Volmer flux ( $\text{m}^{2.5}\text{mol}^{-0.5}\text{s}^{-1}$ )
$i_0$	Scale of Butler Volmer flux for the lithium counter electrode ( $\text{A m}^{-2}$ )
$R$	Universal gas constant, $8.3145 \text{ J mol}^{-1}\text{K}^{-1}$
$k_{c,a}$	Cathodic / anodic rate constant (dimensionless)
$U_0$	Open circuit potential of active material (V)
$\vec{n}$	Normal vector of a surface pointing from solid to electrolyte
$r$	Radial coordinate (m)
$N_{pp}$	Amount of primary particles (dimensionless)
$V_{sp}$	Volume of a secondary particle ( $\text{m}^3$ )
$V_{pp}$	Volume of a primary particle ( $\text{m}^3$ )
$C$	Capacity (As)
$U$	Cell potential (V)
$t$	Time (s)
Greek symbols	Descriptions (Unit)
$\alpha$	Angle between the $b$ and $c$ crystal lattice constants ( $^\circ$ )
$\alpha_{c,a}$	Cathodic / anodic transfer coefficient (dimensionless)
$\Delta\alpha^\circ$	Misalignment angle of the $c$ axis (radian)
$\Delta\alpha$	Misorientation angle of the $a$ $b$ planes of the NMC crystal (radian)
$\beta$	Angle between the $a$ and $c$ crystal lattice constants ( $^\circ$ )

$\gamma$	Angle between the $a$ and $b$ crystal lattice constants ( $^\circ$ )
$\theta$	Polar angle (radian)
$\varphi$	Azimuth angle (radian)
$\varphi_1, \varphi, \varphi_2$	Euler angles based on $zxz$ Bunge convention (radian)
$\mu_{1,2}$	Mean value of Gaussian distribution (dimensionless)
$\sigma_{1,2}$	Standard deviation of Gaussian distribution (dimensionless)
$\rho_e$	Charge density ( $\text{C m}^{-3}$ )
$\kappa$	Ionic conductivity of electrolyte ( $\text{S m}^{-1}$ )
$\varphi_e$	Electrochemical potential (V)
$\phi_s$	Electrical potential in active materials (V)
$\rho_s$	Charge density in active materials ( $\text{C m}^{-3}$ )
$\sigma$	Electrical conductivity of the active material ( $\text{S m}^{-1}$ )
$\eta$	Overpotential (V)

e.g. made of atomically layered lithium nickel manganese cobalt oxide ( $\text{LiNi}_x\text{Mn}_y\text{Co}_{1-x-y}\text{O}_2$ , space group: R 3m, abbr. NMC) or atomically layered lithium nickel cobalt aluminum oxide ( $\text{LiNi}_x\text{Co}_y\text{Al}_{1-x-y}\text{O}_2$ , space group: R 3m, abbr. NCA), which are composed of smaller primary particles (see nanoscale in Fig. 1) usually being single crystals of various sizes, shapes and geometric orientations [9–13]. In addition to these morphological quantities the crystallography of the sub microstructure also plays a crucial role as some important properties, e.g. the diffusion [14,15] and the volume expansion [16–18], are highly anisotropic in layered oxides. Transmission electron microscopy (TEM) measurements locally display the layered nature of these materials but the measurements are limited to a very small region of interest and insufficient for gaining full statistical sampling of a specimen having a size of several microns [10–12]. Apart from these morphological and crystallographical characteristics the presence and location of the grain boundaries, along with the shape, location and orientation of pores between them determine the sub microstructure of a secondary particle entirely. Thus, the sub microstructure regime is described in length scales between the typical dimensions of individual secondary particles ( $\sim 10\text{s } \mu\text{m}$ ) and the appearance of quantum effects ( $\sim 10\text{s nm}$ ). Additional studies show the evolution of the sub microstructure during cycling and the formation of microcracks in secondary particles, leading to capacity loss [11–13,19–23]. Lithium diffusion is strongly affected by the polycrystalline nature of Ni rich NMC secondary particles and their cycling stability improves when the single crystal primary particles, they are composed of, are radially aligned [10–13]. Therefore, it is essential to at least include both the morphology and crystallography when investigating the sub microstructure. Nevertheless in microstructure simulations the sub microstructure is typically neglected and the secondary particles are regarded as composed of homogeneous material, because a more accurate treatment would be too expensive computationally.

In our study we perform electron backscatter diffraction (EBSD) measurements to directly measure the crystallographic orientations in the equatorial plane of polycrystalline NMC622 secondary particles. Contrary to TEM measurements, we thus obtain significant statistical information about the crystallography of samples having sizes of dozens of microns. To the best of our knowledge the analysis of EBSD measurements of cathode materials has only been carried out in the literature with respect to the global Cartesian lab coordinate system [24–28]. Using an evaluation method we developed the EBSD measured orientations are related to a radial reference vector field representing the spherical shape of the NMC secondary particles. This analysis reveals two underlying Gaussian distributions. The dominant peak is likely to result from the radial alignment of the primary particles (longitudinal direction corresponds to a  $b$  plane [11]) whereas the smaller peak probably

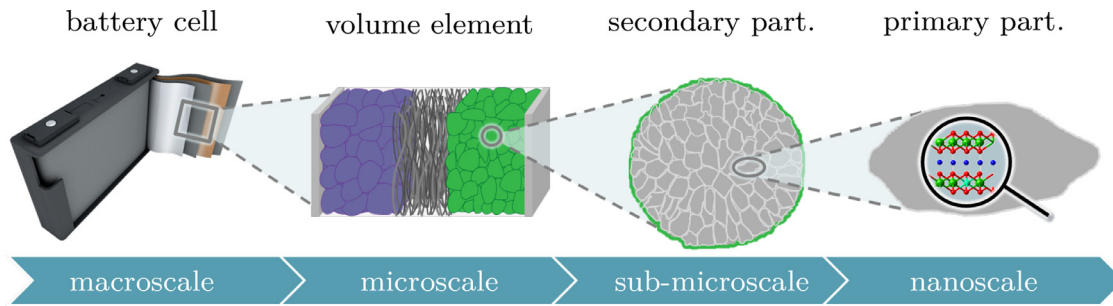


**Fig. 1.** Illustration of the battery cell and its subordinate scales, i.e. the macroscale, the microscale, the sub-microscale and the nanoscale. The primary particles are usually made of single crystals of active material, e.g. NMC or NCA which exhibit a layered atomic structure. The secondary particles result from the arrangement of the primary particles and their morphological and crystallographical configuration. On the microscale the volume elements of the electrodes contain active material particles, binder and additives as well as electrolyte in the void space. The electrodes are separated by a porous polymer that is filled with electrolyte. The battery cell results from the assembly of many anode, separator and cathode layers and some housing.

results from the formation of twin boundaries. Moreover, we perform three dimensional electrochemical simulations, in which a single secondary particle is divided into segments representing the primary particles. We then treat the diffusivity in the individual segments anisotropically representing high diffusivity in the a b plane of the layered oxide and low diffusivity along the c axis. For this anisotropic formulation we finally compare the 1 C discharge capacity of four different cases, i.e. tangential, radial, random and EBSD measurements based, which gives us insights into the influence of the crystallography as one sub microstructure characteristic on the electrochemical behavior.

## 2. Experimental

### 2.1. Material

The experimentally investigated material is commercial NMC622. Therefore there is no information about the synthesis processes, e.g. doping and coating. Nevertheless, Table 1 provides a chemical and physical analysis of the material. The sub microstructure of the NMC secondary particles is shown in Fig. 2a. Those SEM images and the false color images of the EBSD measurements in Fig. 2b and S1 suggest that most primary particles can be regarded as single crystals, as was previously done in the literature [10].

### 2.2. Equipment, setup and measurement

First, we embedded the fractionated NMC622 powder in epoxy resin. Subsequently, a 90° cross section preparation was carried out using the ion beam slope cutting method [29,30] with the EM TIC020 Triple Ion Beam Cutter (Leica Microsystems GmbH, Wien), so that an usable

**Table 1**  
Chemical and physical analysis of the commercial NMC622 powder.

Chemical analysis	
Water [%]	0.005
Cobalt [Mol%]	20.0
Nickel [Mol%]	60.2
Manganese [Mol%]	19.9
Calcium [%]	0.003
Copper [%]	< 0.001
Iron [%]	< 0.001
Sodium [%]	0.029
Physical analysis	
D-10 [ $\mu$ m]	6.3
D-50 [ $\mu$ m]	11.5
D-90 [ $\mu$ m]	19.8

**Table 2**

Lattice parameters used for the EBSD analysis of the NMC sample according to [31].

Lattice parameters	
Space group/-number	R-3mH / 166
a, b [nm]	2.872
c [nm]	14.221
alpha, beta [°]	90
gamma [°]	120

artifact free preparation area of approximately 1.5 mm<sup>2</sup> was prepared for the EBSD measurements.

The analytical scanning electron microscopy was carried out using the FE SEM NVision 40 (Carl Zeiss Microscopy GmbH, Oberkochen). The images were taken using the four quadrant backscattered electron detector at an acceleration voltage of 8 kV (see Fig. 2a).

The EBSD measurements were carried out on the 70° tilted sample using the HKL Nordlys S (Oxford Instruments GmbH, Wiesbaden) EBSD detector at an acceleration voltage of 10 kV. The lattice parameters [31] which were used for the NMC sample for the crystallographic evaluation are shown in Table 2.

For the EBSD measurements only those NMC particles were used, which were cut approximately in the equatorial plane. This was determined based on the particle's size in relationship to neighboring particles. The representation of the crystallographic orientation was carried out via false color images like those in Fig. 2b for specimen 3 and in Fig. S1 for the other specimens where the Euler angles are plotted as false colors. The step size used was in the range of 50 to 80 nm. In total, five different particles were investigated using the EBSD method. From the false color images which refer to the global lab coordinate system no clear regularity or correlation can be seen but the images appear to be colored randomly. Therefore, the next section describes a method for statistically evaluating the orientation data with respect to spherical shape of the secondary particles.

### 2.3. Evaluation method in a spherical context

The atomic structure of NMC622 is represented by the crystallographic space group R 3mH. Thus the atomic structure is invariant with rotations of  $\pi$  around the a or b axis. Because the anisotropic diffusion of lithium in NMC622 is primarily relegated to the {001} planes, the orientations of the [001] axes (along with the Euler angles defined relative to it) play a central role on our analysis of the EBSD measurement. In this section the evaluation method, presented as a flow diagram for specimen 3 in Fig. 3, is presented. The application of this approach to the other specimens is analogous.

The vector field consisting of all vectors  $\vec{u}$  shows the orientation of the measured c axis and is named EBSD vector field  $U \subset \mathbb{R}^3$ . The first

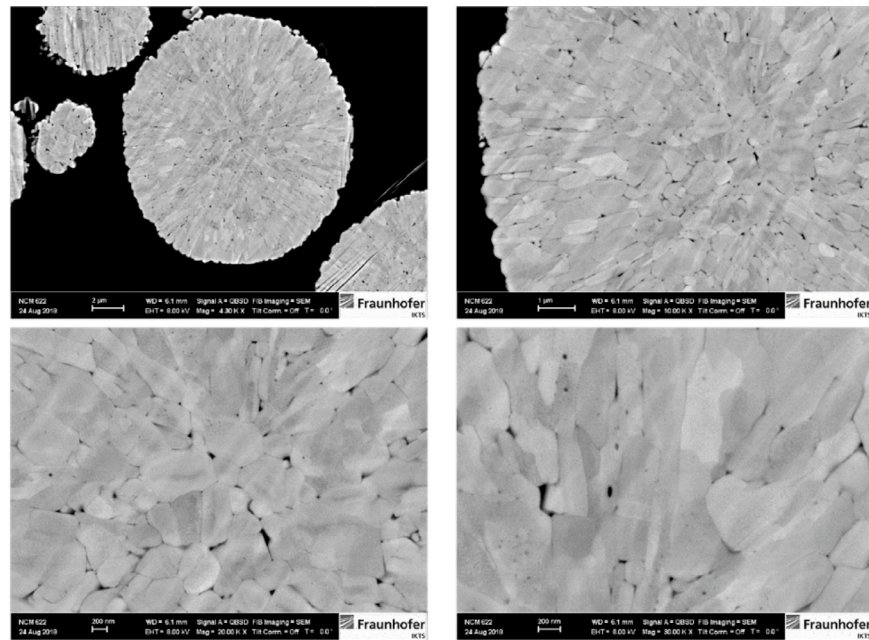
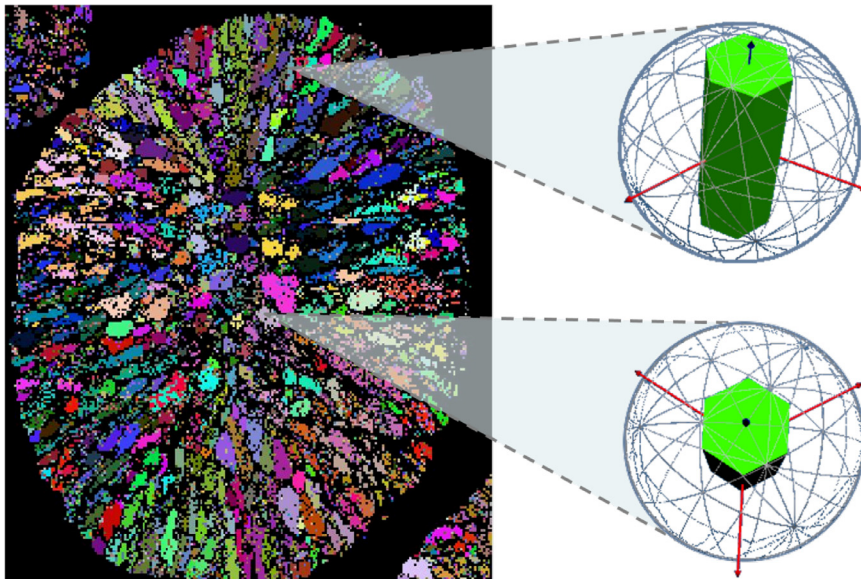


Fig. 2. (a) morphological and (b) crystallographic structure of the investigated NMC622 material.

(a) SEM images of a FIB cross section of a single secondary particle reveal its morphological sub-microstructure, i.e. the secondary particle consists of smaller primary particles which form grain boundaries and pore spaces



(b) The false color image (width of image equals  $15.7\mu\text{m}$ , the particle consists of 20.694 EBSD data points.) of the EBSD measurement of a single secondary particle (specimen 3) displays the measured orientations. The RGB color corresponds to the three Euler angles (Bunge convention) that describe the rotation of the unit cell. Further, two examples show different oriented unit cells (upper example:  $\varphi_1 = 174^\circ$ ,  $\phi = 42^\circ$ ,  $\varphi_2 = 72^\circ$ , lower example:  $\varphi_1 = 177^\circ$ ,  $\phi = 8^\circ$ ,  $\varphi_2 = 0^\circ$ ). The false color images of the other four specimens are displayed in fig. S1.

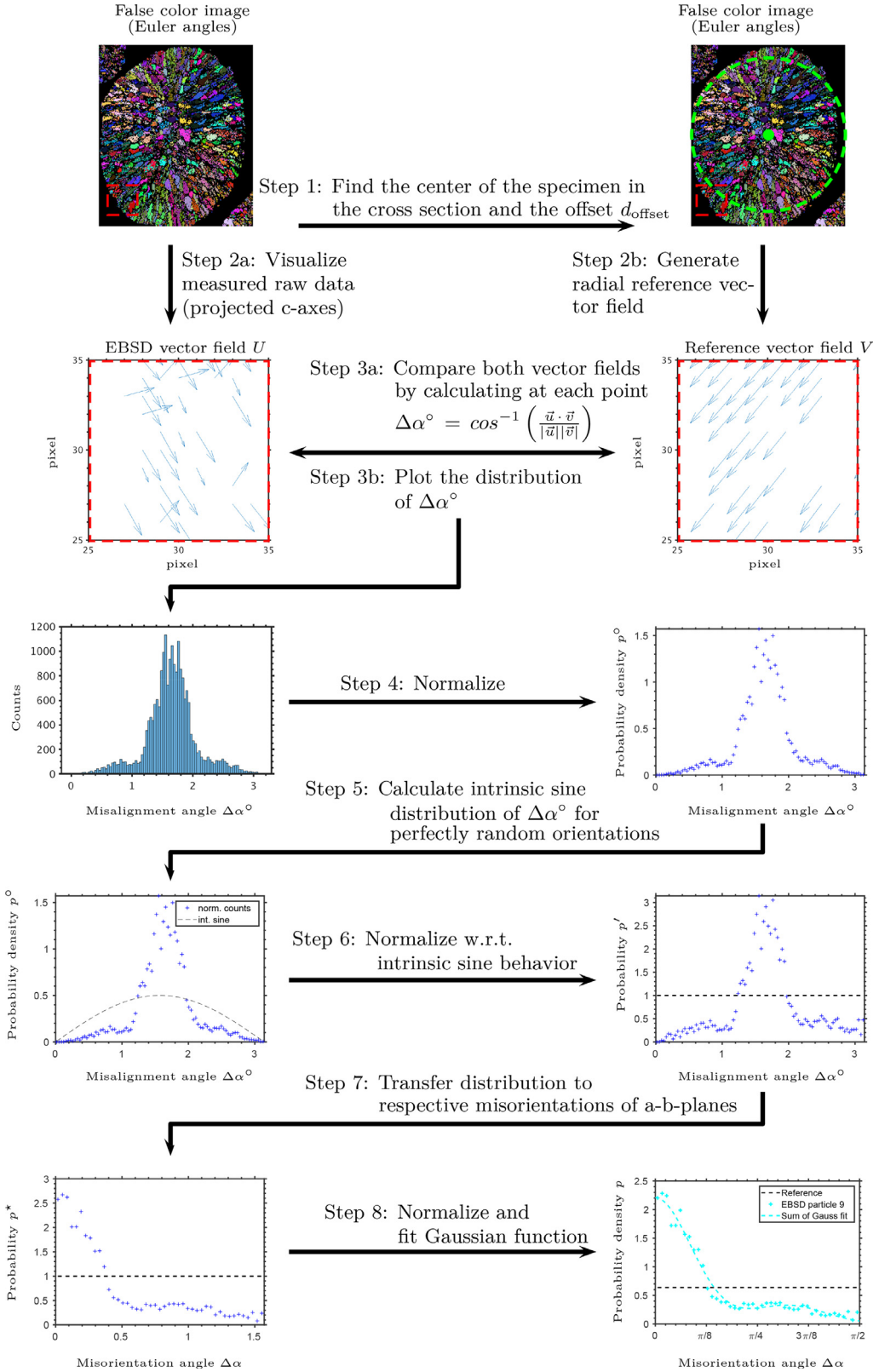


Fig. 3. Flow diagram of the evaluation method described in Section 2.3.

step of evaluating the measurement is to generate a reference vector field by finding the center of the cut particle and creating a respective radial vector field  $V \subset \mathbb{R}^3$ . Then all domains of the two vector fields which do not belong to the region of interest (i.e. parts of neighboring particles) are deleted. Next, the misalignment angle  $\Delta\alpha^\circ$  be

tween each measured c axis and the respective radial vector is calculated by

$$\Delta\alpha^\circ = \cos^{-1}\left(\frac{\vec{u} \cdot \vec{v}}{|\vec{u}||\vec{v}|}\right) \quad (1)$$

and a resulting histogram is gained. This distribution is normalized in order to get the probability density distribution  $p^\circ(\Delta\alpha^\circ)$ . Note that the three dimensional vector  $\vec{u}$  is used and not its projection on the cross section. Further, when assuming the center of the secondary particle lying in the cross section of the experimental setup (i.e. the equatorial plane perfectly equals the cross section) the third component of all vectors  $\vec{v} \in V$  equals zero, which indeed is the case for specimen 3. For all other EBSD measurements it is assumed that the particles are not perfectly cut through their equatorial plane. Thus all vectors  $\vec{v} \in V$  have a non zero third component, whose relative magnitude increases the closer it is to the projected center.

When calculating an infinitesimal annular surface area  $da$  of a sphere using spherical coordinates the area  $da$  is proportional to  $\sin(\Delta\alpha^\circ)$  (see Fig. S4):

$$da = 2\pi R^2 \sin(\Delta\alpha^\circ) d\Delta\alpha^\circ.$$

Regarding  $\vec{v}$  as the radial reference vector and the vector  $\vec{u}$  as the measured orientation of the  $c$  axis it becomes obvious that the intrinsic probability distribution for the misalignment angle of random vectors is sinusoidal. Thus the measured probability density function is related to the density function

$$f(\Delta\alpha^\circ) = 0.5 * \sin(\Delta\alpha^\circ) \quad (2)$$

in order to quantify the deviation of the measured EBSD signal from the intrinsic distribution of random orientations. Thus we get the probability distribution  $p'(\Delta\alpha^\circ)$  when dividing by  $f(\Delta\alpha^\circ)$ :

$$p'(\Delta\alpha^\circ) = p^\circ(\Delta\alpha^\circ) / f(\Delta\alpha^\circ).$$

The last major step of this evaluation is to reinterpret the misalignment angle  $\Delta\alpha^\circ$  in order to directly refer to the diffusion processes. Instead of regarding the angle between the  $c$  axis and the respective radial orientation now it is converted to a misorientation angle  $\Delta\alpha \in [0, \pi/2]$  being the minimum angle between the  $\{001\}$  planes and the radial orientation. Hence, an adapted probability distribution  $p^*$  is obtained by mirroring, renormalizing and shifting  $p'$ :

$$p^*(\Delta\alpha) = \frac{1}{2} \left( p' \left( \frac{\pi}{2} - \Delta\alpha \right) + p' \left( \frac{\pi}{2} + \Delta\alpha \right) \right).$$

By normalizing the distribution  $p^*$  the probability density distribution

$$p(\Delta\alpha) = \frac{p^*(\Delta\alpha)}{\int_0^{\pi/2} p^*(\Delta\alpha') d\Delta\alpha'} \quad (3)$$

can finally be derived. The constant line referring to the expected values for a random orientation distribution (originally sinusoidal) is normalized by dividing by  $\pi/2$ . The probability density distribution  $p(\Delta\alpha)$  is fitted by the function

$$g(\Delta\alpha) = \sum_{i=1}^2 \frac{c_i}{\sqrt{2\pi\sigma_i^2}} \cdot \exp(-(\Delta\alpha - \mu_i)^2 / 2\sigma_i^2) \quad (4)$$

which is the sum of two Gaussian distributions. This finally leads to the plots in Fig. 4 showing the probability density distributions  $p$  of all five specimens with respect to the misorientation angle  $\Delta\alpha$  of the crystal planes as well as the Gaussian fits according to Table 3 and the line referring to the expected distribution of random orientations.

#### 2.4. Results and discussion

Applying the evaluation method described in Section 2.3 to all five particles results in the probability density distributions in Fig. 4. The error based on random noise is expected to be negligible because the data analyses for the five particles are based on 12,832 to 25,379 EBSD data points. The only difference between the evaluation of the particles is the assumed distance  $d_{\text{offset}}$  between the cross section and the actual equatorial plane of the particle. The distances are set to 2.02  $\mu\text{m}$ , 2.05  $\mu\text{m}$ , 0.00  $\mu\text{m}$ , 1.44  $\mu\text{m}$  and 1.30  $\mu\text{m}$  for the specimens 1 to 5, respectively.

**Table 3**

Fitting parameters and root mean square error (RMSE) of the Gaussian fit for each specimen (see Fig. 4) and the mean value and standard deviation (std. dev.) of each fitting parameter.

specimen (SP)	Gaussian distribution parameters						RMSE
	$c_1$	$\mu_1$	$\sigma_1$	$c_2$	$\mu_2$	$\sigma_2$	
SP1	1.24	0.00	0.23	0.39	1.03	0.23	0.061
SP2	1.42	-0.01	0.23	0.34	0.94	0.40	0.115
SP3	1.56	-0.01	0.28	0.23	1.02	0.29	0.103
SP4	1.56	0.00	0.25	0.23	1.01	0.25	0.112
SP5	0.91	0.00	0.23	0.48	1.00	0.32	0.198
SP-mean	1.34	0.00	0.25	0.33	1.00	0.30	-
SP-std. dev.	0.27	0.004	0.02	0.11	0.034	0.07	-

In order to compare the Gaussian fits, the fitting parameters of all particles as well as their mean values and standard deviations are summarized in Table 3. Further, the table contains the root mean square error (RMSE) for each set of fitting parameters, which quantifies the quality of the fits by applying the formula

$$\text{RMSE} = \sqrt{\frac{1}{N} \sum_{i=1}^N (G_i - P_i)^2}$$

where  $N$  is the total amount of data points,  $G_i$  the predicted value from the Gaussian curve and  $P_i$  the observed value from the EBSD measurement. From the RMSE values in Table 3 it becomes clear that the probability density distributions can be described by the Gaussian function (4) very well. Comparing the RMSE values with each other it can be seen that the precision of the fits is roughly always the same. Thus, it is convenient to compare the fitting parameters, which is done by calculating the mean value and the respective standard deviation of each parameter. Hence, we find out that for all investigated NMC622 particles the probability density distribution of the misorientation angle  $\Delta\alpha$  can be approximately described by the relation

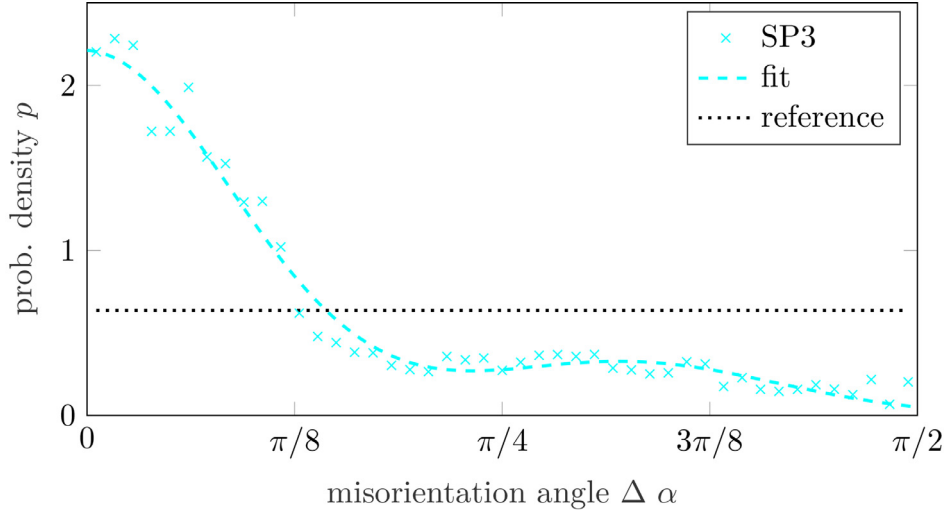
$$g(\Delta\alpha) = 2.15 \cdot e^{-\left(\frac{\Delta\alpha}{0.35}\right)^2} + 0.45 \cdot e^{-\left(\frac{\Delta\alpha-1.00}{0.42}\right)^2} \quad (5)$$

which is plotted in Fig. 5. This leads to the interpretation of having two statistical processes with respect to the crystallographic orientation during the formation of the sub microstructure where each process has an underlying Gaussian statistic. On the one hand, this is probably the arrangement process of the elongated primary particles as densely packed spherical secondary particle. The cyan pixel in Fig. S3 cause the  $\mu_1$  Gaussian peak and they tend to form elongated and radial aligned areas. Especially, the third particle which is perfectly cut through the equatorial plane shows these features. On the other hand, the crystallization process during calcination at high temperatures has a severe impact on the morphology and crystallography of the primary crystals [13] and likely results in the formation of twin boundaries, which has been observed in Ni rich NMC [13,32]. When evaluating the misorientations at the boundaries of our primary particles (see Fig. S2) we find distinct peaks at grain boundary angles of 60° and 90° for all five particles. Fig. S3 highlights these two kinds of grain boundaries and further displays the pixel that cause the  $\mu_2$  peak in the Gaussian distribution. Searching for clusters or regions with a high density of these pixel shows that they are often located close to the 90° grain boundaries or are situated in grains adjacent to these grain boundaries. Thus, it seems likely that the  $\mu_2$  peak results from the reported twin boundaries. These findings based on the spatial distribution of the respective data points support our hypotheses about the origin of the two Gaussian peaks.

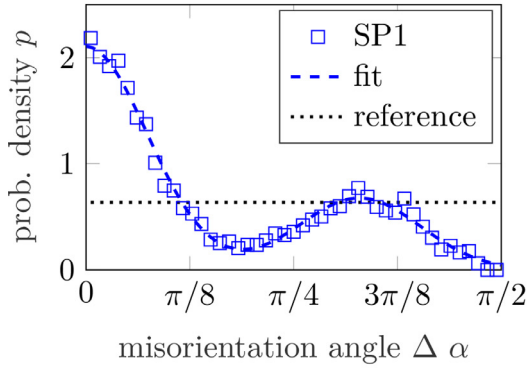
Due to the shapes of the fitted Gaussian distributions we denote the investigated particles as crystallographically radial. In each case the shape is characterized by

$$c_1 \gg c_2, \quad \mu_1 \approx 0, \quad \sigma_1 \approx 0.25$$

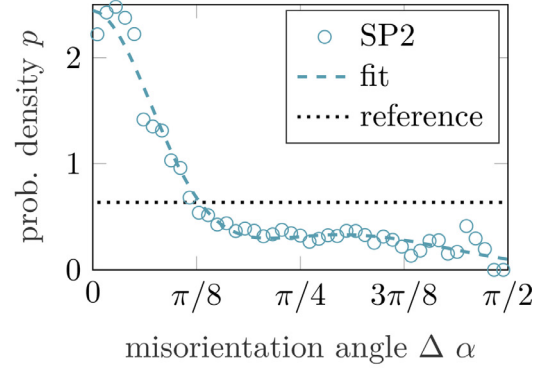
These aspects finally result in probabilities of 56 %, 67 %, 69 %, 70 % and 48 % of having a misorientation angle in the interval  $[0; \pi/8]$  for the



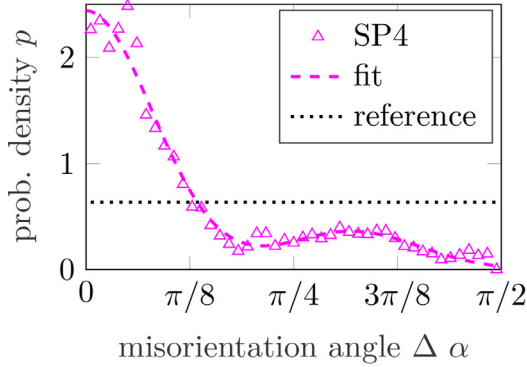
(a) Specimen 3 (SP3)



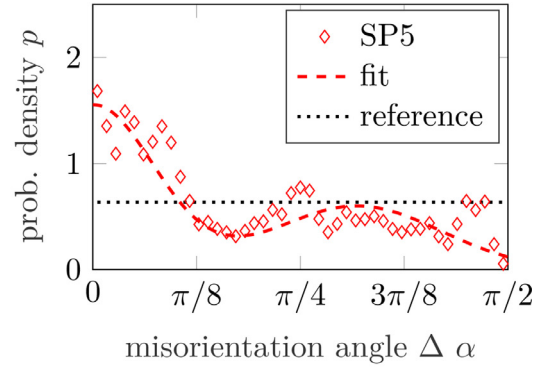
(b) Specimen 1 (SP1)



(c) Specimen 2 (SP2)



(d) Specimen 4 (SP4)



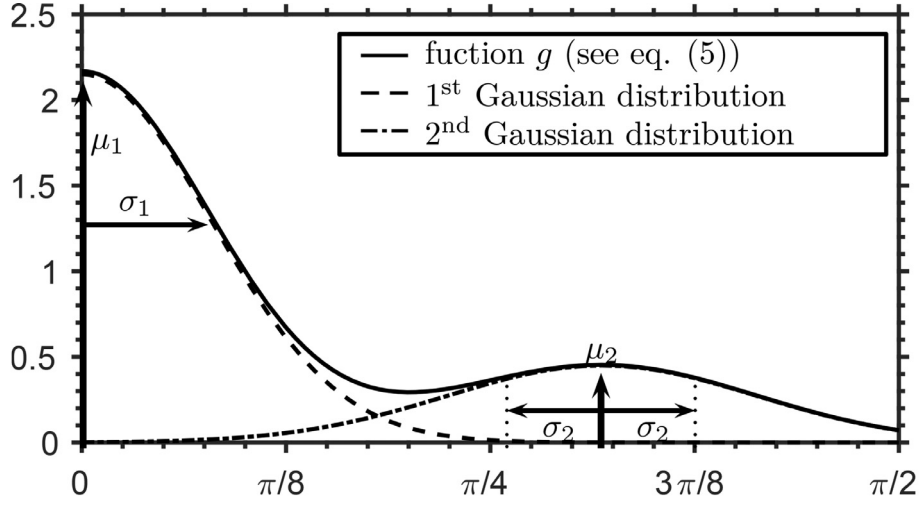
(e) Specimen 5 (SP5)

**Fig. 4.** Final probability density distributions of the specimens SP1 to SP5 and the respective Gaussian fits according to Eq. (4). The constant dotted line at  $2/\pi$  corresponds to the probability density distribution of perfectly random distributed orientations. The respective false color images are displayed in Fig. 2b and Fig. S1.

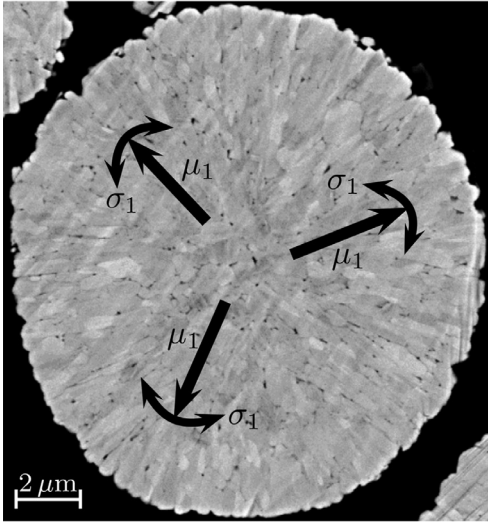
specimens 1 through 5, respectively, whereas a probability of only 25 % is expected in the case of randomly oriented primary grains.

The evaluation method of this experimental part was developed independently from Xu et al. [33] but shows great similarities regarding the first steps. However, there is one crucial difference regarding the evaluated data. Whereas Xu et al. analyzed the gradient field of the Ni valence state distribution, from which only indirectly crystal orientations

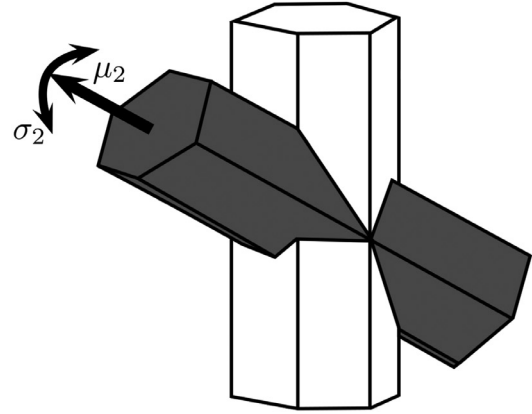
are estimated in combination with very local TEM images, we directly evaluate the crystal orientation of a cross section, which gives us more statistical evidence regarding crystal orientations. Both studies complement each other very well so that more detailed statistical information can be obtained and a bunch of hypotheses can be concluded. Assuming the primary particles in rod NMC (nomenclature used by Xu et al.) as elongated ellipsoids both the longest half axis (morphological consider



(a) Plot of the function (5) which is the sum of two Gaussian distributions



(b) 1<sup>st</sup> statistical process



(c) 2<sup>nd</sup> statistical process

**Fig. 5.** (a) depicts the overall probability density distribution that results from the sum of two Gaussian distributed processes each of them having a dedicated mean and standard deviation. (b) visualizes the first statistical process being the radial alignment of the primary particles. (c) visualizes the second statistical process being the formation of twin boundaries.

ation) and the a b plane of the crystal (crystallographical consideration) are oriented equally, which corresponds to [11]. Moreover, performing spatially resolved TXM like Xu et al. gives sophisticated insights into charge distribution but it seems like the gradient field of the Ni valence state distribution does not indicate the direction of lithium flux (according to Fick's law), which seems counter intuitive at the first glance but reasonable in detail. The vector field rather displays either the directions of diffusion barriers, i.e. the c direction of the NMC crystal (like proposed by Kan et al. [34].), or the normal vector of the grain boundaries as lithium ions might accumulate at the grain boundaries (like proposed by Sui et al. [35]). Furthermore, in our mind the gravel NMC (nomenclature used by Xu et al.) looks more homogeneous whereas the rod NMC exhibits distinct radial domains with high oxidation state. But yet the overall state of charge is the same for the gravel and rod NMC so that we assume similar effective diffusion velocities for different ratios of bulk and grain boundary diffusion. In addition, as the gravel NMC seems to be more homogeneous we conclude that the main cause of mechanical stress and particle cracking is not the different magnitudes of

the concentration gradient in rod and gravel NMC but rather the different crystallographic orientations that lead to more or less synchronized volume expansions.

Finally, in our experiments pure NMC is investigated, but from our experience we would expect other materials to be feasible for these kind of EBSD measurements, too. Both cathode and anode active materials as well as composite materials should be suitable as long as crystalline regions exist and exceed the microscope's resolution, i.e. in our case roughly about 50 nm. Hence, we expect much new research information on morphological and crystallographic aspects when applying our evaluation method to other energy storage materials.

### 3. Simulations

#### 3.1. 3D Electrochemical model

The electrochemical model used in this paper is based on a thermodynamically consistent model [36,37]. This model is applicable to

three dimensional structures and thus to investigations of the secondary particle's sub microstructure. The investigated volume element of the lithium ion battery cell is very small and contains only one secondary particle. Thus all processes are regarded as isothermal, which finally results in the governing equations (6) to (9) describing the system. We used the COMSOL Multiphysics® software to perform the simulations [38].

### 3.1.1. Electrolyte

For the electrolyte this model neglects both convection as it is highly unlikely and charge separation as scales above 20 nm are regarded so that the electrochemical double layer around the active particle is not resolved. Furthermore, a binary salt is used as electrolyte, which results in some simplifications of the transport equations. Thus from the thermodynamic consistent model we finally get

$$\begin{aligned} \partial_t c_e &= -\vec{\nabla} \cdot \vec{N}_+ \\ &= \vec{\nabla} \cdot (D_e \vec{\nabla} c_e) - \vec{\nabla} \cdot \left( \frac{t_+}{z_+ F} \vec{j} \right) \end{aligned} \quad (6)$$

from the mass balance. Here  $c_e$  is the lithium concentration in the electrolyte,  $N_+$  the flux of lithium ions,  $\vec{j}$  the electrical current,  $D_e$  the diffusion coefficient for the electrolyte,  $t_+$  the transference number of the lithium ions,  $z_+$  the charge number of the lithium ions and  $F$  the Faraday constant. From charge conservation we further get

$$\begin{aligned} \partial_t \rho_e &= 0 = -\vec{\nabla} \cdot \vec{j} \\ &= \vec{\nabla} \cdot (\kappa \vec{\nabla} \varphi_e) - \vec{\nabla} \cdot \left( \kappa \frac{1-t_+}{z_+ F} \left( \frac{\partial \mu}{\partial c_e} \right) \vec{\nabla} c_e \right) \end{aligned} \quad (7)$$

where  $\rho_e$  is the charge density,  $\varphi_e$  the electrochemical potential and  $\kappa$  the ionic conductivity.

### 3.1.2. Active material

For the active material mass balance as well as charge conservation are regarded. Contrary to the electrolyte it is assumed that the electrical current only results from electronic and not ionic contribution so that  $t_+ = 0$ . Thus we obtain

$$\begin{aligned} \partial_t c_s &= -\vec{\nabla} \cdot \vec{N}_+ \\ &= \vec{\nabla} \cdot (D_s \vec{\nabla} c_s) \end{aligned} \quad (8)$$

$$\begin{aligned} \partial_t \rho_s &= 0 = -\vec{\nabla} \cdot \vec{j} \\ &= \vec{\nabla} \cdot (\sigma \vec{\nabla} \phi_s) \end{aligned} \quad (9)$$

with  $c_s$  being the lithium concentration,  $\phi_s$  the electrical potential,  $D_s$  the diffusion coefficient,  $\rho_s$  the charge density and  $\sigma$  the electrical conductivity. In each case the subscript s indicates that this is a property of the solid phase.

In our simulations we focus on the lithium transport processes in polycrystalline cathode active materials. Thus, only one single secondary particle is regarded and its primary particles are resolved by dividing a three dimensional sphere along the spherical coordinates into individual segments. Furthermore, the diffusion is modeled as anisotropic with a high diffusivity within the a b planes and a reduced diffusivity in c direction. Rotated, local coordinates are assigned to each segment and hence it is possible to realize different crystallographic orientation distributions. For details about modeling the sub microstructure of a secondary particle see section S2 in the supplementary information.

### 3.1.3. Interface conditions

At the interface between the solid and liquid phase the intercalation reaction takes place. The resulting flux  $i_{se}$  is usually described by the Butler Volmer equation

$$i_{se} = i_0 \left[ \exp \left( \frac{\alpha_a F}{RT} \eta_s \right) - \exp \left( \frac{-\alpha_c F}{RT} \eta_s \right) \right] \quad (10)$$

**Table 4**

Simulation parameters. Since the parameters for NMC111 and for LiPF<sub>6</sub> in EC/DMC are known quite well most values are taken from the literature.

electrolyte	
$\kappa/\text{Sm}^{-1}$	0.98 [39]
$t_+/-$	0.4 [39]
$D_e/\text{m}^2\text{s}^{-1}$	$2.72 \cdot 10^{-10}$ [39]
$(1 + \partial \ln f_c / \partial \ln c_e)/-$	2.191 [40]
$c_0/\text{molm}^{-3}$	1000 [39]
$\varphi_{e,0}/\text{V}$	0
NMC electrode	
$\sigma/\text{Sm}^{-1}$	0.023 [41]
$D^*/\text{m}^2\text{s}^{-1}$	$2 \cdot 10^{15}$ [42]
$i_{00}/\text{m}^2\text{s}^{-1}$	$5.06 \cdot 10^{-6}$ [43]
$c_s^{\text{max}}/\text{molm}^{-3}$	36224 [43]
$\alpha_a/-$	0.5 [3]
$\alpha_c/-$	0.5 [3]
$U_0/\text{V}$	cf[43].
$\text{SOC}_0/-$	0.2
Li counter electrode	
$i_0/\text{Am}^{-2}$	10 [44]
$\alpha_a/-$	0.5
$\alpha_c/-$	0.5
$U_0/\text{V}$	0
$\phi_s/\text{V}$	0

$$\begin{aligned} &= F(k_c)^{\alpha_a} (k_a)^{\alpha_c} (c_s^{\text{max}} - c_s)^{\alpha_a} c_s^{\alpha_c} c_e^{\alpha_a} \\ & * \left[ \exp \left( \frac{\alpha_a F}{RT} \eta_s \right) - \exp \left( \frac{-\alpha_c F}{RT} \eta_s \right) \right] \end{aligned} \quad (11)$$

where the overpotential  $\eta_s$  is defined by

$$\eta_s = \phi_s - \varphi_e - U_0 \quad (12)$$

with  $U_0$  being the open circuit potential of the active material,  $\varphi_e$  the electrochemical potential of the electrolyte and  $\phi_s$  the electrical potential of the solid phase. Further,  $k_c$ ,  $\alpha_c$ ,  $k_a$ ,  $\alpha_a$ ,  $c_s^{\text{max}}$ ,  $R$  and  $T$  are the cathodic rate constant and transfer coefficient, the anodic rate constant and transfer coefficient, the maximum lithium concentration in the active material, the universal gas constant and the temperature, respectively. Since no side reactions and no formation of the electrochemical double layer is modeled we get the following interfacial conditions

$$\vec{j}_s \cdot \vec{n} = i_{se} \quad (13)$$

$$\vec{j}_e \cdot \vec{n} = i_{se} \quad (14)$$

$$\vec{N}_{+,s} \cdot \vec{n} = \frac{i_{se}}{z_+ F} \quad (15)$$

$$\vec{N}_{+,e} \cdot \vec{n} = \frac{i_{se}}{z_+ F} \quad (16)$$

where  $\vec{n}$  is the surface normal pointing from the solid to so liquid phase.

For our simulations the material parameters refer to a solution of LiPF<sub>6</sub> in ethylene carbonate (EC) and dimethyl carbonate (DMC) which is hosted in a polyvinylidene fluoride (PVDF) separator. As cathode active material NMC111 is chosen since the respective material properties have been investigated for a long time and are known quite well. All simulation parameters including material properties, initial and boundary conditions are listed in Table 4.

**Table 5**

Simulated discharge capacities of the secondary particle for different cases. Since 40 simulations are performed for the random and EBSD statistics based cases, statistical values are calculated, i.e. the mean, standard deviation (std.), minimum (min.) and maximum (max.) value.

case\capacity / $\mu\text{As}$	mean	std.	min.	max.
isotropic	0.993	-	-	-
radial	0.993	-	-	-
tangential	0.085	-	-	-
random	0.829	0.028	0.777	0.870
EBSD statistics	0.891	0.019	0.860	0.920

### 3.2. Results and discussion

In this section we regard five fundamental different cases, i.e. the radial, the tangential, the random and the EBSD based one and further the results for an isotropic diffusion parameter  $D_s = D^*$ . The isotropic simulation serves as reference because most 3D models and the radial formulation of the P2D model correspond to an isotropic diffusion process.

Note that the model does not contain any aging mechanisms and is reversible. Therefore the following statements hold true for both charging and discharging. Here we focus on discharging currents of 1 C. According to the volume of the spherical secondary particle  $V_{\text{SecPart}}$ , its theoretical maximum lithium concentration density  $c_{s,\text{max}}$  (see Table 4) and a utilization factor of 80% the maximum capacity is  $C_{\text{max}} = V_{\text{SecPart}} \cdot c_{s,\text{max}} \cdot 0.80 \cdot F = 2,227 \mu\text{As}$ . Further, note that so far no grain boundary diffusion is implemented into the model. This will be part of future investigations to verify to what extent the following statements hold true when grain boundary diffusion is also considered. From the experimental observations in Section 2 and the lack of published information we assume that it will be hard to estimate the impact of grain boundaries on the diffusion. It is difficult to experimentally quantify grain boundary diffusion and from our experimental observations we further assume different kinds of grain boundaries which can be for instance seen in the statistics on the angles between grains (see Fig. S2) and in the SEM images (see. fig. 2). Therefore some grain boundaries might be rather regarded as interfaces between primary particles that can be hardly seen as classical grain boundary. Hence, there might be different kinds of interfaces when it comes to diffusion processes. Nevertheless, we relate our following results to a potential impact of grain boundary diffusion.

Simulating the aforementioned five different cases whereby the random and EBSD based cases are performed for 40 different realizations results in the discharge curves shown in Fig. 6a. The respective capacities at the end of discharge (with an upper and lower cutoff potential of 4.2 V and 3.0 V, respectively) are summarized in Table 5. Furthermore, Fig. 6 illustrates the lithium concentration and flux for the different cases at the end of discharge as color map and vector field, respectively.

From these information several conclusions can be drawn. First, the isotropic and radial cases show very similar lithiation processes. Therefore it seems convenient to simplify the microscopic behavior by an isotropic diffusion mechanism if the secondary particles are almost spherical and the diffusion occurs in perfectly radial pathways (neglecting the impact of grain boundaries which are not aligned in radial directions). These two cases do not refer to real configurations of polycrystalline particles but they rather serve as reference or limiting cases. It turns out that the perfectly radial orientation of the a b planes show the highest capacity in our simulations. Thus, this case represents the best case scenario and reveals the theoretical improvements that can be achieved. On the other hand, the isotropic case refers to another limiting case that shows similar electrochemical performance like the perfect radial one. These two limiting cases are shown as they correspond to the assumptions of most battery cell models, e.g. the P2D model.

In addition, the tangential case represents the worst case scenario as almost no diffusion into the particle takes place, which for sure is emphasized by the missing grain boundary diffusion. This case is far away from physically realistic configurations but is also simulated to complete the picture and give some idea about a possible worst case arrangement of the primary particles.

The random and the EBSD statistics cases represent the physically most realistic cases. They show varying behavior depending on the exact realization of the statistics. The capacities of the random and EBSD cases vary with respect to their mean value by  $\pm 6\%$  and  $\pm 3\%$ , respectively. The standard deviation correspond to 3% and 2%, respectively. Thus, it seems reasonable to understand the sub microstructure effects on the overall performance in detail. The concentration and flux field in Fig. 6e display that the random crystallographic orientations lead to varying concentration profiles along different radial directions. In contrast, Fig. 6i shows a rather regular lithium distribution for the EBSD case, which finally leads to higher capacities.

Furthermore, the EBSD based cases shows in average about 8% higher capacities than the random cases. This shows that the sub microstructure of the NMC particles is already designed in an optimized way or as discussed in the experimental part this optimized crystallographic structure is thermodynamically more favorable. But as many boundary conditions of the synthesis processes have to be set by the supplier, which probably affect the thermodynamics (e.g. temperature, pH value), it is rather convenient that these parameters are part of the supplier's knowledge. This is encouraged by several experimental studies [10,45,46] that show the impact of the synthesis process on the sub microstructure. Hence, an thermodynamically and thus intrinsically preferred orientation distribution is only valid for certain sets of boundary conditions during synthesis.

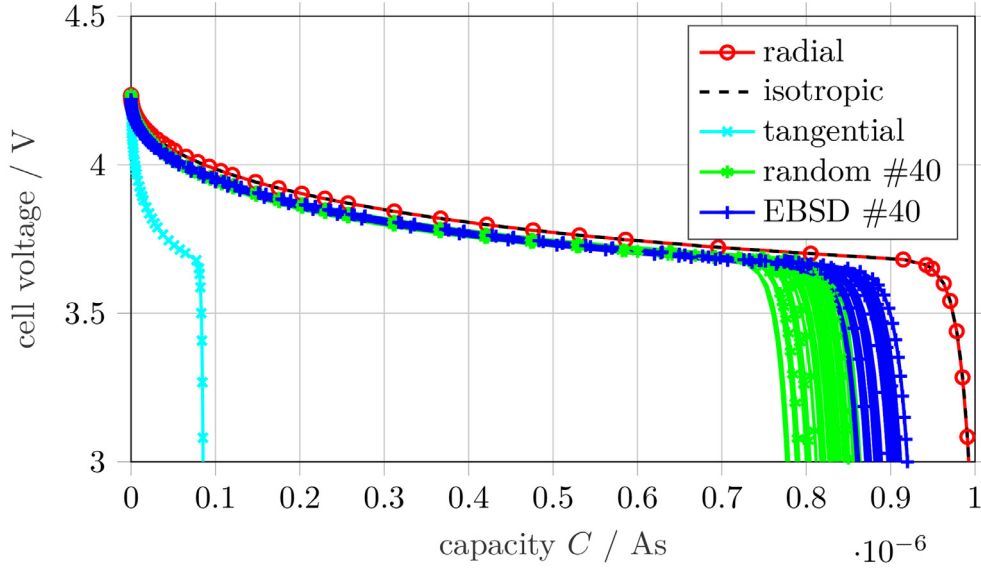
From figure 7c in the supplementary information of the study [33] one can estimate a difference in the specific capacity between gravel and rod NMC811 of about  $(193 - 179)/179 \approx 7.8\%$ . These galvanostatic measurements give experimental evidence for the impact of the morphological and crystallographic configuration and is in good agreement with our simulations. Nevertheless, including more realistic morphologies and grain boundary effects in our model will give further insights into the transport processes inside polycrystalline secondary particles.

In addition, comparing the mean value of the EBSD statistics based capacities with the one of the perfectly radial aligned primary grains, it is shown that further optimizations of the sub microstructure are still possible. Eventually, this results in an increment of the cyclable capacity of about 11%.

Our investigations focus on the secondary particles' capacities due to anisotropic diffusivity and varying crystallographic orientations. Since the volume expansion is also highly anisotropic with abrupt changes in the c lattice parameter other investigations further show enhanced mechanical stability if there is a radial structure of the primary particles [11,13,33]. The anisotropic volume changes are more pronounced for Ni rich NMCs and lead to enhanced capacity loss [47]. When investigating the mechanical behavior of polycrystalline secondary particles, in our opinion, it must be clearly distinguished between the morphology and the crystallography as well. We expect a strong impact of both the morphology and especially the crystallography on the mechanical behavior and thus on aging mechanisms.

## 4. Conclusions

In this study we show that crystal orientations can be directly measured with high precision using EBSD by performing measurements on cross sections of five NMC secondary particles. The evaluation of the measurements in a spherical context shows that most crystals are oriented radially, i.e. the local radial direction of the spherical secondary particle lies in the a b plane of the primary grains. For all five specimens the orientation distribution can be fitted by the sum of two Gaussian



(a) Discharge curves of the different cases (see fig. S6) reveal that the orientation distribution of the local coordinate systems affects the capacity severely. Having the same statistics but different realizations results in varying capacities of  $\pm 6\%$  and  $\pm 3\%$  for the random and EBSD based statistics, respectively.

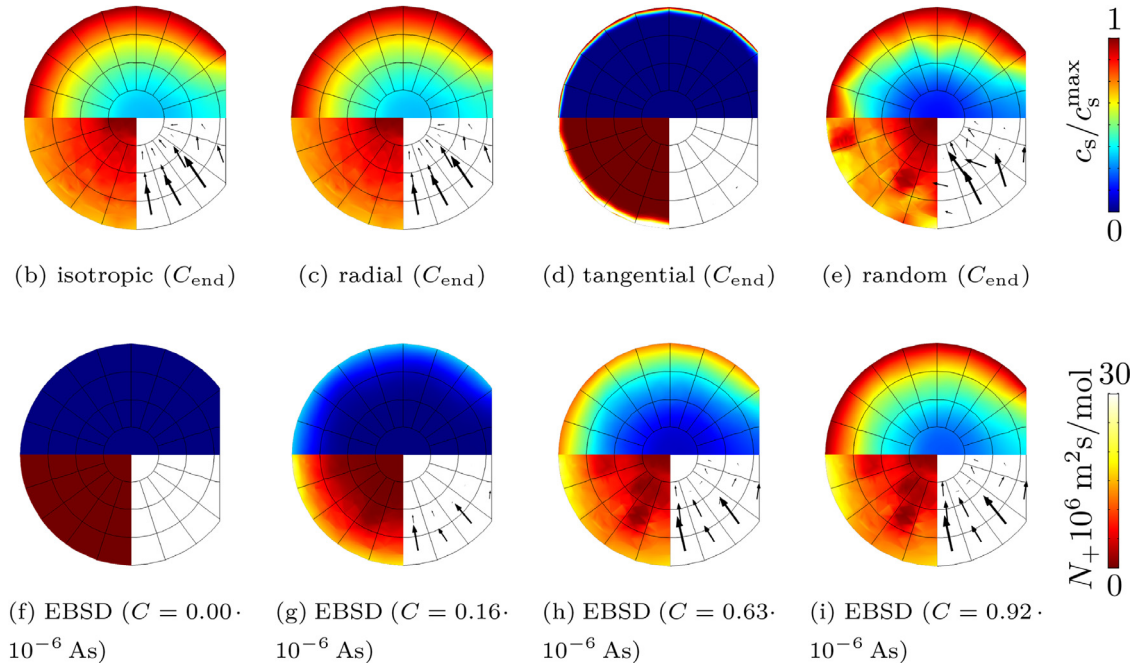


**Fig. 6.** Plot (a) shows the discharge curves of all simulations. The plots (b-i) depict the normalized lithium concentration in the first and second quadrant, the magnitude of lithium flux in the third quadrant and the lithium flux as vector field in the fourth quadrant. Figures (b-e) and (i) show the respective information for the time step that corresponds to the end of discharge whereas (f-h) illustrate intermediate time steps. (c-e) and (f-i) are the same cases that are plotted in Fig. S6. Additionally, (b) displays the result for an isotropic diffusion tensor where the diffusion process is independent from the local coordinate systems. The color bars are valid for all plots.

functions, which when averaged, result in the following probability distribution function:  $g(\Delta\alpha) = 2.15 \cdot e^{-\left(\frac{\Delta\alpha}{0.35}\right)^2} + 0.45 \cdot e^{-\left(\frac{\Delta\alpha-1.00}{0.42}\right)^2}$ . The two Gaussian like peaks can be attributed to the dominant radial alignment of the elongated primary grains and to the formation of thermodynamically stable twin boundaries. This result for the crystallographic orientations is very well reproduced in all five measurements with very similar

fitting parameters for the two Gaussians. Obviously, this is an indication that the crystallization kinetics during synthesis are very reproducible. All in all, we directly observe a distinct radial orientation of the primary grains in a crystallographic and not a morphological sense.

Although grain boundary diffusion is ignored so far our simulations already indicate that the crystallography severely impacts the ca

capacity of NMC secondary particles. This effect mainly comes from the anisotropic lithium diffusion which results in a lithium flux along the *a* and *b* planes within NMC materials. Furthermore, we have shown that commercial NMC already exhibits an advanced sub microstructure that enables higher capacities than random crystallographic orientations. In average the experimentally measured particles show 8% higher capacities than randomly oriented ones. But still the capacity of the commercial NMC might be enhanced by an additional 11% if the crystallographic orientations were to be perfectly radial. These simulations show that commercial NMC already have advantageous crystallographic configurations. However, further fine tuning of the radial diffusion paths during material synthesis still allows considerable improvements to be made.

## Declaration of Competing Interest

The authors declare that they have no known competing financial interests or personal relationships that could have appeared to influence the work reported in this paper.

## CRediT authorship contribution statement

**Julian Wegener:** Conceptualization, Methodology, Software, Formal analysis, Writing original draft, Visualization. **Levin Chee Xian Ho:** Software, Formal analysis, Visualization. **Vedran Glavas:** Conceptualization, Supervision, Project administration, Writing review & editing. **Jonathan Edward Mueller:** Supervision, Writing review & editing. **Sören Höhn:** Investigation, Writing original draft. **André Clausner:** Project administration. **Arnulf Latz:** Conceptualization, Supervision, Writing review & editing.

## Acknowledgment

The authors thank Volkswagen AG for the financial support of this work. The results, opinions and conclusions expressed in this publication are not necessarily those of Volkswagen Aktiengesellschaft.

We further would like to thank Natalija Guschanski at University of Applied Sciences and Arts of Hanover for her collaboration and discussion. The authors also acknowledge the discussion with Börn Matthey on grain boundaries.

## References

- [1] Press release: The Nobel Prize in Chemistry 2019, Nobel-Prize.org, Nobel Media AB 2020, Mon. 11 May 2020., 2019, (URL <https://www.nobelprize.org/prizes/chemistry/2019/press-release>).
- [2] M. Doyle, T.F. Fuller, J. Newman, Modeling of galvanostatic charge and discharge of the lithium/polymer/insertion cell, *J Electrochem Soc* 140 (6) (1993) 1526–1533, doi:10.1149/1.2221597. <http://jes.ecsdl.org/content/140/6/1526.abstract>.
- [3] T.F. Fuller, M. Doyle, J. Newman, Simulation and optimization of the dual lithium ion insertion cell, *J Electrochem Soc* 141 (1) (1994) 1–10, doi:10.1149/1.2054684.
- [4] D. Schmidt, M. Kamlah, V. Knoblauch, Highly densified NCM-cathodes for high energy li-ion batteries: microstructural evolution during densification and its influence on the performance of the electrodes, *Journal of Energy Storage* 17 (2018) 213–223, doi:10.1016/j.est.2018.03.002.
- [5] H. Kang, C. Lim, T. Li, Y. Fu, B. Yan, N. Houston, V.D. Andrade, F.D. Carlo, L. Zhu, Geometric and electrochemical characteristics of  $\text{LiNi}_{1/3}\text{Mn}_{1/3}\text{Co}_{1/3}\text{O}_2$  electrode with different calendaring conditions, *Electrochim. Acta* 232 (2017) 431–438, doi:10.1016/j.electacta.2017.02.151.
- [6] C.-M. Chu, C.-Y. Liu, Y.-Y. Wang, C.-C. Wan, C.-R. Yang, On the evaluation of the factors influencing the rate capability of a  $\text{LiCoO}_2/\text{Li}$  battery, *J. Taiwan Inst. Chem. Eng.* 43 (2) (2012) 201–206, doi:10.1016/j.jtice.2011.10.015.
- [7] F.-Y. Su, L.-Q. Dai, X.-Q. Guo, L.-J. Xie, G.-H. Sun, C.-M. Chen, Micro-structure evolution and control of lithium-ion battery electrode laminate, *Journal of Energy Storage* 14 (2017) 82–93, doi:10.1016/j.est.2017.09.016.
- [8] A. Shodiev, E. Primo, O. Arcelus, M. Chouchane, M. Osenberg, A. Hilger, I. Manke, J. Li, A.A. Franco, Insight on electrolyte infiltration of lithium ion battery electrodes by means of a new three-dimensional-resolved lattice boltzmann model, *Energy Storage Materials* 38 (2021) 80–92, doi:10.1016/j.ensm.2021.02.029.

- [9] H.-J. Noh, S. Yoon, C.S. Yoon, Y.-K. Sun, Comparison of the structural and electrochemical properties of layered  $\text{Li}[\text{Ni}_x\text{Co}_y\text{Mn}_{1-x-y}]\text{O}_2$  ( $x = 1/3, 0.5, 0.6, 0.7, 0.8, 0.85$ ) cathode material for lithium-ion batteries, *J Power Sources* 233 (2013) 121–130, doi:10.1016/j.jpowsour.2013.01.063.
- [10] X. Xu, H. Huo, J. Jian, L. Wang, H. Zhu, S. Xu, X. He, G. Yin, C. Du, X. Sun, Radially oriented single-Crystal primary nanosheets enable ultrahigh rate and cycling properties of  $\text{LiNi}_{0.8}\text{Co}_{0.1}\text{Mn}_{0.1}\text{O}_2$  cathode material for lithium-ion batteries, *Adv Energy Mater* 9 (15) (2019) 1803963, doi:10.1002/aenm.201803963.
- [11] U.-H. Kim, H.-H. Ryu, J.-H. Kim, R. Mücke, P. Kaghazchi, C.S. Yoon, Y.-K. Sun, Microstructure-Controlled Ni-rich cathode material by microscale compositional partition for next-Generation electric vehicles, *Adv Energy Mater* 9 (15) (2019) 1803902, doi:10.1002/aenm.201803902.
- [12] C.S. Yoon, K.-J. Park, U.-H. Kim, K.H. Kang, H.-H. Ryu, Y.-K. Sun, High-Energy Ni-rich  $\text{Li}[\text{Ni}_x\text{Co}_y\text{Mn}_{1-x-y}]\text{O}_2$  cathodes via compositional partitioning for next-Generation electric vehicles, *Chem. Mater.* 29 (24) (2017) 10436–10445, doi:10.1021/acs.chemmater.7b04047.
- [13] U.-H. Kim, G.-T. Park, B.-K. Son, G.W. Nam, J. Liu, L.-Y. Kuo, P. Kaghazchi, C.S. Yoon, Y.-K. Sun, Heuristic solution for achieving long-term cycle stability for Ni-rich layered cathodes at full depth of discharge, *Nat. Energy* 5 (11) (2020) 860–869, doi:10.1038/s41560-020-00693-6.
- [14] F. Fu, G.-L. Xu, Q. Wang, Y.-P. Deng, X. Li, J.-T. Li, L. Huang, S.-G. Sun, Synthesis of single crystalline hexagonal nanobricks of  $\text{LiNi}_{1/3}\text{Mn}_{1/3}\text{O}_2$  with high percentage of exposed 010 active facets as high rate performance cathode material for lithium-ion battery, *J. Mater. Chem. A* 1 (2013) 3860–3864, doi:10.1039/C3TA01618H.
- [15] D. Luo, G. Li, C. Fu, J. Zheng, J. Fan, Q. Li, L. Li,  $\text{LiMO}_2$  (M=Mn, Co, Ni) hexagonal sheets with (101) facets for ultrafast charging-discharging lithium ion batteries, *J Power Sources* 276 (2015) 238–246, doi:10.1016/j.jpowsour.2014.11.122.
- [16] E.-J. Lee, Z. Chen, H.-J. Noh, S.C. Nam, S. Kang, D.H. Kim, K. Amine, Y.-K. Sun, Development of microstrain in aged lithium transition metal oxides, *Nano Lett.* 14 (8) (2014) 4873–4880, doi:10.1021/nl5022859. PMID: 24960550
- [17] B.-B. Lim, S.-T. Myung, C.S. Yoon, Y.-K. Sun, Comparative study of Ni-rich layered cathodes for rechargeable lithium batteries:  $\text{Li}[\text{Ni}_{0.85}\text{Co}_{0.11}\text{Al}_{0.04}]\text{O}_2$  and  $\text{Li}[\text{Ni}_{0.84}\text{Co}_{0.06}\text{Mn}_{0.09}\text{Al}_{0.01}]\text{O}_2$  with two-step full concentration gradients, *ACS Energy Lett.* 1 (1) (2016) 283–289, doi:10.1021/acsenenergyl.6b00150.
- [18] L. de Biasi, A.O. Kondrakov, H. Geüweint, T. Brezesinski, P. Hartmann, J. Janek, Between scylla and charybdis: balancing among structural stability and energy density of layered ncm cathode materials for advanced lithium-ion batteries, *The Journal of Physical Chemistry C* 121 (47) (2017) 26163–26171, doi:10.1021/acs.jpcc.7b06363.
- [19] D.J. Miller, C. Proff, J.G. Wen, D.P. Abraham, J.B. no, Observation of microstructural evolution in li battery cathode oxide particles by in situ electron microscopy, *Adv Energy Mater* 3 (8) (2013) 1098–1103, doi:10.1002/aenm.201300015.
- [20] S. Watanabe, M. Kinoshita, T. Hosokawa, K. Morigaki, K. Nakura, Capacity fade of  $\text{LiAl}_x\text{Ni}_{1-x}\text{Co}_y\text{O}_2$  cathode for lithium-ion batteries during accelerated calendar and cycle life tests (surface analysis of  $\text{LiAl}_x\text{Ni}_{1-x}\text{Co}_y\text{O}_2$  cathode after cycle tests in restricted depth of discharge ranges), *J Power Sources* 258 (2014) 210–217, doi:10.1016/j.jpowsour.2014.02.018.
- [21] H.-R. Kim, S.-G. Woo, J.-H. Kim, W. Cho, Y.-J. Kim, Capacity fading behavior of Ni-rich layered cathode materials in li-ion full cells, *J. Electroanal. Chem.* 782 (2016) 168–173, doi:10.1016/j.jelechem.2016.10.032.
- [22] Z. Xu, M.M. Rahman, L. Mu, Y. Liu, F. Lin, Chemomechanical behaviors of layered cathode materials in alkali metal ion batteries, *J. Mater. Chem. A* 6 (2018) 21859–21884, doi:10.1039/C8TA06875E.
- [23] R. Ruess, S. Schweidler, H. Hemmelmann, G. Conforto, A. Bielefeld, D.A. Weber, J. Sann, M.T. Elm, J. Janek, Influence of NCM particle cracking on kinetics of lithium-ion batteries with liquid or solid electrolyte, *J Electrochem Soc* 167 (10) (2020) 100532, doi:10.1149/1945-7111/ab9a2c.
- [24] J.R. Wilson, J.S. Cronin, S.A. Barnett, S.J. Harris, Measurement of three-dimensional microstructure in a  $\text{LiCoO}_2$  positive electrode, *J Power Sources* 196 (7) (2011) 3443–3447, doi:10.1016/j.jpowsour.2010.04.066.
- [25] J. Li, A.R. Cameron, H. Li, S. Glazier, D. Xiong, M. Chatzidakis, J. Allen, G.A. Botton, J.R. Dahn, Comparison of single crystal and polycrystalline  $\text{LiNi}_{0.5}\text{Mn}_{0.3}\text{Co}_{0.2}\text{O}_2$  positive electrode materials for high voltage li-ion cells, *J Electrochem Soc* 164 (7) (2017) A1534–A1544, doi:10.1149/2.0991707jes.
- [26] J.-H. Shim, C.-Y. Kim, S.-W. Cho, A. Missiul, J.-K. Kim, Y.J. Ahn, S. Lee, Effects of heat-treatment atmosphere on electrochemical performances of Ni-rich mixed-metal oxide ( $\text{LiNi}_{0.80}\text{Co}_{0.15}\text{Mn}_{0.05}\text{O}_2$ ) as a cathode material for lithium ion battery, *Electrochim. Acta* 138 (2014) 15–21, doi:10.1016/j.electacta.2014.06.079.
- [27] D. Zeibig, T. Bernthaler, G. Schneider, S. Freitag, Visualization of crystal orientation and the granulate sub-Grain size in lithium ion batteries by means of EBSD and correlative microscopy, *Microsc. Microanal.* 24 (S1) (2018) 1512–1513, doi:10.1017/S1431927618008048.
- [28] G. Qian, Y. Zhang, L. Li, R. Zhang, J. Xu, Z. Cheng, S. Xie, H. Wang, Q. Rao, Y. He, Y. Shen, L. Chen, M. Tang, Z.-F. Ma, Single-crystal nickel-rich layered-oxide battery cathode materials: synthesis, electrochemistry, and intra-granular fracture, *Energy Storage Materials* 27 (2020) 140–149, doi:10.1016/j.ensm.2020.01.027.
- [29] W. Hauffe, Device for preparing the substance samples for investigation, 1977, (????).
- [30] R. Behrisch, K. Wittmaack, Sputtering by particle bombardment III, volume 64, 1991, doi:10.1007/3-540-53428-8.
- [31] P. Yue, Z. Wang, H. Guo, F. Wu, Z. He, X. Li, Effect of synthesis routes on the electrochemical performance of  $\text{Li}[\text{Ni}_{0.6}\text{Co}_{0.2}\text{Mn}_{0.2}]\text{O}_2$  for lithium ion batteries, *J. Solid State Electrochem.* 16 (12) (2012) 3849–3854, doi:10.1007/s10008-012-1823-3.
- [32] S. Li, Z. Yao, J. Zheng, M. Fu, J. Cen, S. Hwang, H. Jin, A. Orlov, L. Gu, S. Wang, Z. Chen, D. Su, Direct observation of defect-aided structural evolution in

- a nickel-rich layered cathode, *Angew. Chem. Int. Ed.* 59 (49) (2020) 22092–22099, doi:10.1002/anie.202008144.
- [33] Z. Xu, Z. Jiang, C. Kuai, R. Xu, C. Qin, Y. Zhang, M.M. Rahman, C. Wei, D. Nordlund, C.-J. Sun, X. Xiao, X.-W. Du, K. Zhao, P. Yan, Y. Liu, F. Lin, Charge distribution guided by grain crystallographic orientations in polycrystalline battery materials, *Nat Commun* 11 (1) (2020) 83, doi:10.1038/s41467-019-13884-x.
- [34] W.H. Kan, B. Deng, Y. Xu, A.K. Shukla, T. Bo, S. Zhang, J. Liu, P. Pianetta, B.-T. Wang, Y. Liu, G. Chen, Understanding the effect of local short-Range ordering on lithium diffusion in  $\text{Li}_{1.3}\text{Nb}_{0.3}\text{Mn}_{0.4}\text{O}_2$  single-Crystal cathode, *Chem* 4 (9) (2018) 2108–2123, doi:10.1016/j.chempr.2018.05.008.
- [35] T. Sui, B. Song, J. Dluhos, L. Lu, A.M. Korsunsky, Nanoscale chemical mapping of li-ion battery cathode material by FIB-SEM and TOF-SIMS multi-modal microscopy, *Nano Energy* 17 (2015) 254–260, doi:10.1016/j.nanoen.2015.08.013.
- [36] A. Latz, J. Zausch, Thermodynamic consistent transport theory of li-ion batteries, *J Power Sources* 196 (6) (2011) 3296–3302, doi:10.1016/j.jpowsour.2010.11.088.
- [37] A. Latz, J. Zausch, Multiscale modeling of lithium ion batteries: thermal aspects, *Beilstein J Nanotechnol* 6 (2015) 987–1007, doi:10.3762/bjnano.6.102.
- [38] COMSOL Multiphysics®v. 5.5. [www.comsol.com](http://www.comsol.com). COMSOL AB, Stockholm, Sweden
- [39] D. Djian, F. Alloin, S. Martinet, H. Lignier, Macroporous poly(vinylidene fluoride) membrane as a separator for lithium-ion batteries with high charge rate capacity, *J Power Sources* 187 (2) (2009) 575–580, doi:10.1016/j.jpowsour.2008.11.027.
- [40] L.O. Valøen, J.N. Reimers, Transport properties of  $\text{LiPF}_6$ -Based li-Ion battery electrolytes, *J Electrochem Soc* 152 (5) (2005) A882–A891, doi:10.1149/1.1872737.
- [41] S.-H. Kang, J. Kim, M. Stoll, D. Abraham, Y. Sun, K. Amine, Layered  $\text{Li}(\text{Ni}_{0.5-x}\text{Mn}_{0.5-x}\text{M}_{2x})\text{O}_2$  ( $\text{M}=\text{co, al, ti; } x=0, 0.025$ ) cathode materials for li-ion rechargeable batteries, *J Power Sources* 112 (1) (2002) 41–48, doi:10.1016/S0378-7753(02)00360-9.
- [42] D.W. Dees, D.P. Abraham, W. Lu, K.G. Gallagher, M. Bettge, A.N. Jansen, Electrochemical modeling and performance of a lithium- and manganese-Rich layered transition-Metal oxide positive electrode, *J Electrochem Soc* 162 (4) (2015) A559–A572, doi:10.1149/2.0231504jes.
- [43] T. Danner, M. Singh, S. Hein, J. Kaiser, H. Hahn, A. Latz, Thick electrodes for li-ion batteries: a model based analysis, *J Power Sources* 334 (2016) 191–201, doi:10.1016/j.jpowsour.2016.09.143.
- [44] S.G. Meibuhr, Electrode studies in nonaqueous electrolytes, *J Electrochem Soc* 117 (1) (1970) 56, doi:10.1149/1.2407438.
- [45] L. Wang, X. He, W. Sun, J. Wang, Y. Li, S. Fan, Crystal orientation tuning of  $\text{LiFePO}_4$  nanoplates for high rate lithium battery cathode materials, *Nano Lett.* 12 (11) (2012) 5632–5636, doi:10.1021/nl3027839. PMID: 23074971
- [46] J. Kim, H. Ma, H. Cha, H. Lee, J. Sung, M. Seo, P. Oh, M. Park, J. Cho, A highly stabilized nickel-rich cathode material by nanoscale epitaxy control for high-energy lithium-ion batteries, *Energy Environ. Sci.* 11 (2018) 1449–1459, doi:10.1039/C8EE00155C.
- [47] H.-H. Ryu, K.-J. Park, C.S. Yoon, Y.-K. Sun, Capacity fading of Ni-rich  $\text{li}[\text{nixcoymnlxy}]_2$  ( $0.6 \leq x \leq 0.95$ ) cathodes for high-energy-density lithium-ion batteries: bulk or surface degradation? *Chem. Mater.* 30 (3) (2018) 1155–1163, doi:10.1021/acs.chemmater.7b05269.